


 Cite this: *Lab Chip*, 2018, 18, 1057

A robust tissue laser platform for analysis of formalin-fixed paraffin-embedded biopsies†

 Yu-Cheng Chen,^a Qiushu Chen,^a Xiaoqin Wu,^a Xiaotian Tan,^a Juanhong Wang^b and Xudong Fan^{a*}

Laser emission-based detection and imaging technology has attracted significant interest in biomedical research due to its high sensitivity, narrow linewidth, and superior spectral and spatial resolution. Recent advances have further revealed the potential to use laser emission to investigate chromatin dynamics, as well as to diagnose cancer tissues based on nuclear biomarkers. To move the laser emission based detection technology a step further towards practical use, in this work, we developed a highly robust tissue laser platform by microfabricating an SU8 spacer with a fixed height on the top mirror of the Fabry-Pérot (FP) cavity, which allows generation of reproducible and stable lasing results regardless of tissue thickness. Then we applied this platform to achieve lasing emission from formalin-fixed, paraffin-embedded (FFPE) lung tissues, which account for an overwhelming fraction of tissues collected for research and clinical use worldwide. We further showed that the cancer and normal FFPE lung tissues can be distinguished by their respective lasing thresholds. Two different tissue thicknesses (10 μm and 5 μm) commonly used in pathological labs were explored. Finally, we tested three additional types of tissues (colon, stomach, and breast) that were prepared independently by lab technicians in a pathology lab in China and shipped to the US in order to validate the general applicability and practicality of the laser emission-based technology as well as the corresponding sample preparation protocol and the tissue laser platform. Our work will not only vastly broaden the applications of laser emission-based detection/imaging technology but also help translate it from the laboratory to an automated system for clinical practice that may eventually benefit biomedicine and biological research.

 Received 23rd January 2018,
Accepted 26th February 2018

DOI: 10.1039/c8lc00084k

rsc.li/loc

1. Introduction

Laser-based detection has emerged as a novel tool in biosensing, biomedical research, and diagnosis due to its capability to amplify subtle changes in gain media caused by underlying biological processes.^{1–14} Laser emission has unique advantages over fluorescence, including narrow linewidth, threshold behavior, and strong intensity,^{7,15} leading to ultrasensitive detection,^{16,17} superior image contrast,^{18–20} and higher spectral/spatial resolution.^{4,20} Recently, laser emission-based microscopy has been employed in screening lung cancer tissues from human patients.²⁰ It is found that the cancer cells have a significantly lower lasing threshold than normal cells, which allows for differentiating cancer and normal tissues with high sensitivity and specificity. These results promise potential applications of the laser emission-based detec-

tion in cancer screening,^{21,22} tumor grading and subtyping, and immunodiagnostics.²⁰

To move the laser emission-based detection technology a step further towards practical use, it is critical that the following questions or issues are answered or addressed. First, in a previous work, only cryogenic frozen tissues were used. However, frozen tissues are hard to preserve and the ice crystal formation may create artifacts during diagnosis. As an alternative to frozen tissues, the overwhelming majority of tissues are stored in the form of formalin-fixed, paraffin-embedded (FFPE) tissues with well over 400 million FFPE tissue samples assembled in biorepositories.²³ FFPE tissues are known for their convenience, cost-effectiveness, long-term preservation ability, and valuable resource in clinical pathology,²⁴ cancer prognosis, translational genomics, and proteomic research.^{25–27} However, it is unclear whether the laser characteristics will be significantly affected by strongly scattering and opaque matrix materials (e.g., paraffin) and whether we are still able to differentiate the cancer and normal FFPE tissues by their lasing thresholds, as demonstrated previously in cryogenic samples. Second, we need to develop a reliable system and protocols that are compatible with the general practice in a pathological lab and that

^a Department of Biomedical Engineering, University of Michigan, 1101 Beal Ave, Ann Arbor, MI, 48109, USA. E-mail: xsfan@umich.edu

^b Department of Pathology, Xi'an No. 3 Hospital, No. 10, Feng Cheng 3rd Road, Xi'an, Shaanxi, 710018, P. R. China

† Electronic supplementary information (ESI) available. See DOI: 10.1039/c8lc00084k

can be used conveniently by a lab technician to generate reproducible results and yet not to damage tissue samples. Finally, in addition to the lung tissues used in the previous work, it is important to investigate whether our technology can be generally applicable to other types of tissues (such as colon, stomach, and breast tissues).

In this work, we developed a highly robust lasing emission-based imaging and detection platform by microfabricating an SU8 spacer with a fixed height on the top mirror of the Fabry–Pérot (FP) cavity, which is able to generate reproducible results regardless of the tissue thickness. In addition, the top mirror can be removed and placed back repetitively so that regular bright-field and fluorescence images can be acquired along with the laser emission-based images. We further used lung FFPE tissues as a model system to study the lasing characteristics from those tissues and investigate the feasibility to differentiate cancer and normal lung tissues based on their respective lasing thresholds. Two different tissue thicknesses (10 μm and 5 μm) commonly used in pathological labs were explored. Finally, we tested three additional types of tissues (colon, stomach, and breast) that were prepared independently by lab technicians in a pathology lab in China and shipped to the US in order to validate the general applicability and practicality of the laser emission-based technology as well as the corresponding sample preparation protocol and the lasing imaging/detection system. This work will not only vastly broaden the applications of laser emission-based detection/imaging technology but also help translate it from the laboratory to an automated system for clinical practice that may eventually benefit biomedicine and biological research.

2. Experimental

Tissue preparation and staining

In this study, a total of 30 FFPE tissue samples from 20 patients' tissues were used, including human lung tissues, co-

lon tissues, stomach tissues, and breast tissues, all of which were obtained under IRB approved by the institutional committees and the informed consent forms were obtained. Detailed information of all the tissues used in this work is described in Table S1.† All the human lung tissues used and shown in Fig. 1–6 were purchased from OriGene Technologies in the form of FFPE tissue blocks. Both male and female patients diagnosed with stage I/II cancer, with ages from 40 to 75, were examined. Samples were collected from a diverse set of medical institutions throughout the United States in order to maximize patient diversity. These tissues were verified at the company by pathologists with full pathological evaluation data, clinical annotation (including patient age, gender, and minimum stage grouping), and abstracted pathology reports to ensure the accuracy of the sample level diagnosis. For human lung tissues (shown in Fig. S5†) and colon, stomach, and breast FFPE tissues (shown in Fig. 7), they were collected from Asian patients and prepared by lab technicians in a pathology lab in Xi'an No. 3 Hospital, China. The bottom mirrors were first shipped from the US to China for tissue preparation and mounting and then shipped back to the US for laser measurements.

For the samples prepared at the University of Michigan, all FFPE tissue blocks were sliced into 10 μm or 5 μm thick sections by using a microtome (Thermo Fisher #HM355S). The selected tissue section was picked up, rinsed in a 45 °C warm water-bath, and then placed on the top of a poly-L-lysine (Sigma-Aldrich #P8920) coated dielectric mirror, which was first cleaned and rinsed with lysine for better tissue adhesion. The tissues were then soaked in xylene for 5 minutes to clean off the paraffin and wax materials. Then the tissues were soaked in different concentrations of ethanol, 100%, 95%, 75%, and 50%, each for 2 minutes. Next, the tissues were soaked and rinsed with DI water and PBS (phosphate buffer solution, ThermoFisher #10010023) and air dried before staining (see staining/labeling details in the next

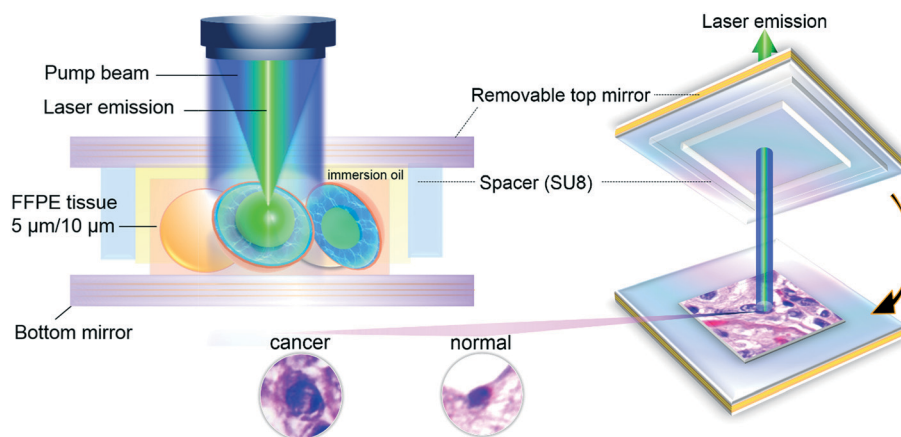


Fig. 1 Conceptual illustration of an FFPE tissue laser platform, in which formalin-fixed paraffin-embedded (FFPE) tissue is sandwiched within a high-Q Fabry–Pérot (FP) cavity and the top mirror is removable and reusable. A spacer is microfabricated on the top mirror in order to fix the FP cavity length. Refractive index matching oil is used to reduce the reflection caused by the gap between the tissue and the top mirror. For this work, the spacer was made of SU8 and was designed to be 15 μm . The tissue thickness was 5 μm and 10 μm , respectively. The sample was excited by a pulsed laser at 470 nm.

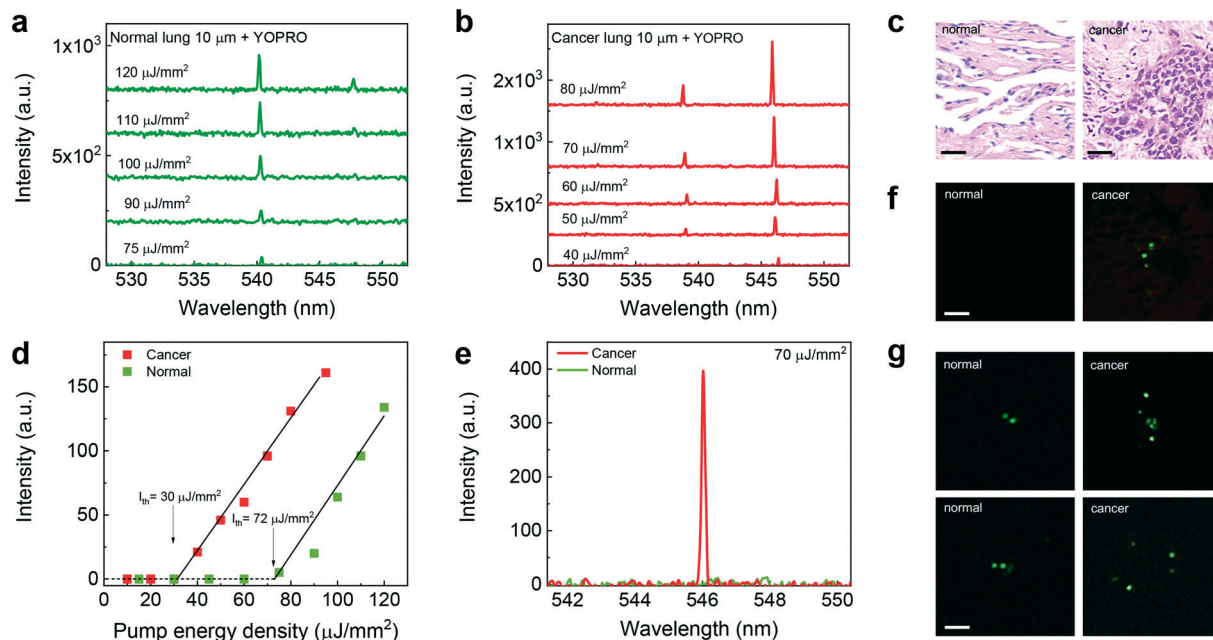


Fig. 2 a, Examples of lasing spectra of the normal lung tissue (10 μm in thickness) stained with YOPRO (0.1 mM) under various pump energy densities. b, Examples of lasing spectra of the lung cancer tissue (10 μm) stained with YOPRO (0.1 mM) under various pump energy densities. All curves are vertically shifted for clarity. Excitation wavelength = 470 nm. Numerical aperture = 0.42. Cavity length = 15 μm . The slight blueshift in a and b is the result of the photobleaching effect. c, H&E images of representative normal and cancer tissues used in this work. Scale bars, 60 μm . d, Spectrally integrated laser output as a function of pump energy density extracted from the laser spectra of the normal and cancer tissues. The solid lines are the linear fit above the lasing threshold, which was 30 $\mu\text{J mm}^{-2}$ and 72 $\mu\text{J mm}^{-2}$ for the cancer and normal tissues, respectively. e, Direct comparison of laser emission spectra of normal (green curve) and cancer (red curve) lung FFPE tissues (10 μm in thickness) under a pump energy density of 70 $\mu\text{J mm}^{-2}$. f, Laser emission images of normal and cancer cells when pumped around 70 $\mu\text{J mm}^{-2}$. Scale bar, 10 μm . g, Representative laser emission images taken from normal and cancer tissues with multiple lasing cells when pumped around 100 $\mu\text{J mm}^{-2}$. Scale bar, 10 μm .

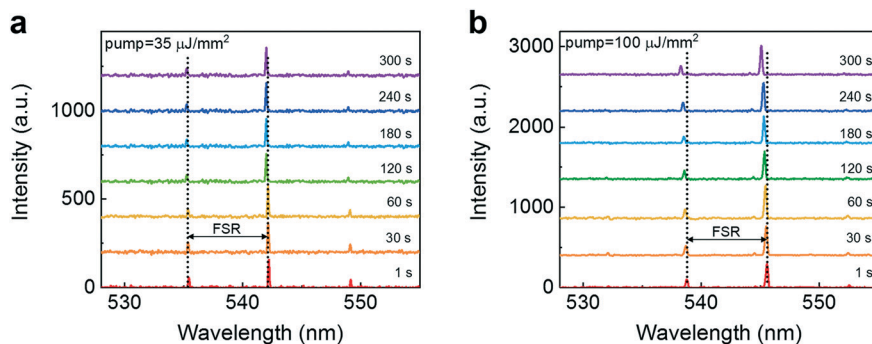


Fig. 3 a, Time series lasing spectra of the cancer lung FFPE tissue (10 μm in thickness) labeled with YOPRO. All spectra were measured under the same pump energy density of 35 $\mu\text{J mm}^{-2}$. b, Time series lasing spectra of the normal lung FFPE tissue (10 μm in thickness) labeled with YOPRO. All spectra were measured under the same pump energy density of 100 $\mu\text{J mm}^{-2}$. Cavity length = 15 μm . The free spectral range (FSR) is 6.8 nm and 6.9 nm for the cancer and normal tissues, respectively. Curves are vertically shifted for clarity. The vertical lines in a and b are used to guide the eye. A slight blueshift (a total of 0.45 nm in 5 minutes) in the lasing wavelength in b may result from the dye photobleaching at a relatively high pump energy density (*i.e.*, 100 $\mu\text{J mm}^{-2}$).

paragraph). Finally, the tissues were covered with the top mirror. Refractive index matching immersion oil ($n = 1.42$) (ThermoFisher #S36937), which is commonly used in microscopy, was used to fill the gap between the tissue and the top mirror. For the samples prepared in the pathological lab in China, the same protocol was followed to mount the tissue sections (all 5 μm in thickness) onto the bottom mirrors. For experiments in Fig. 4, 6 and 7, all of the tissues were sec-

tioned into 2 slices and at least 10 cells within the tumor/normal region from each tissue section were randomly selected and measured. The number of cells picked up and measured depends on how many cells can express lasing in a certain fixed area on each tissue, which is strongly affected by the density of the cells and tissue types. For all cases, we require a minimum of 10 positive lasing cells per tissue slice for effective comparison and biological significance.

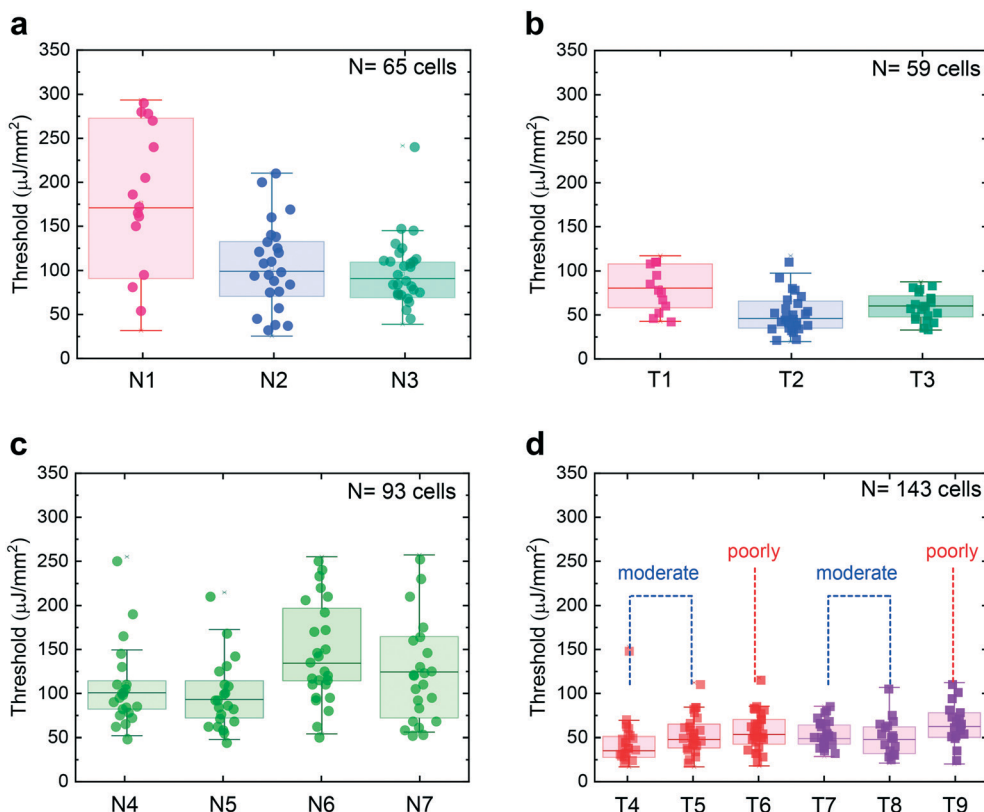


Fig. 4 a, Statistics of the lasing threshold for cells in the normal tissues stained with YOPRO (labeled N1–N3) from three matched-paired patients. b, Statistics of the lasing threshold for cells in the cancer lung tissues stained with YOPRO (labeled T1–T3) from the same three patients in a. c, Statistics of the lasing threshold for cells in the normal lung tissues stained with YOPRO (labeled N4–N7) from four individual (nonmatched-paired) patients. d, Statistics of the lasing threshold for cells in the cancer lung tissues stained with YOPRO (labeled T4–T9) from six different lung cancer patients (with moderately or poorly differentiated cells). In a–d, each dot represents the lasing data from a single cell. Statistical box plots are also shown in a–d. In d, the red box stands for squamous cell carcinoma, while the purple box stands for adenocarcinoma. Exemplary H&E microscopy images of the two major types of non-small cell lung cancers, including squamous cell carcinoma for T4–T6 and adenocarcinoma for T7–T9, are shown in Fig. S3† All tissues were 10 μm in thickness sandwiched in a cavity length (with a spacer) of 15 μm . [YOPRO] = 0.1 mM for all samples.

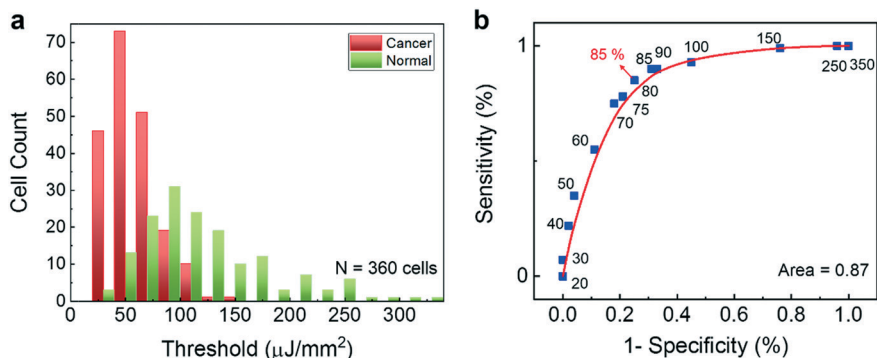


Fig. 5 a, Histogram of all cancer/normal cell lasing thresholds ($N = 360$) extracted from Fig. 4. b, Receiver operating characteristic (ROC) curve based on the 360 cells. The ROC curve is plotted by using the different excitations (denoted by the numbers of the dots in units of $\mu\text{J mm}^{-2}$) as the cut-off criterion. The area under the fitted red curve is 0.87 and a sensitivity of 85% is obtained based on the criterion of 80 $\mu\text{J mm}^{-2}$.

For nucleic acid labeling, YOPRO solution (ThermoFisher #Y3603) was dissolved in PBS to form a concentration of 0.1 mM. The prepared YOPRO solution was then applied to the tissue sections for 10 minutes and rinsed with PBS solution twice before measurements.

FP cavity and spacer fabrication

The FP cavity was formed by two customized dielectric mirrors (Fig. S1†) made by Evaporated Coatings Inc. (Willow Grove, PA, USA). They had high reflectivity in the spectral

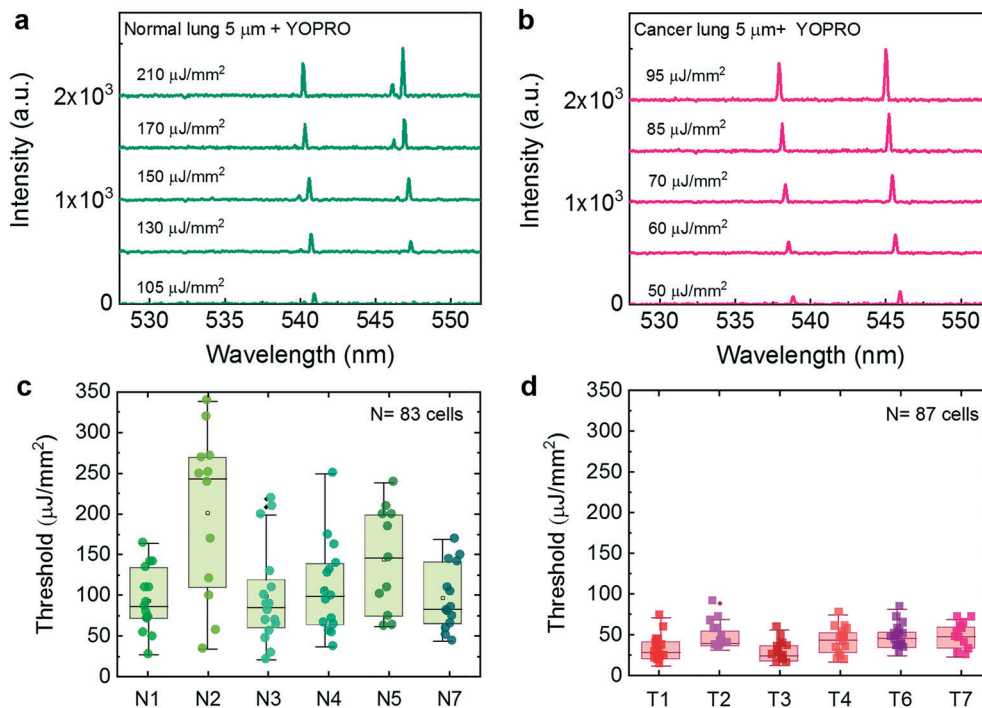


Fig. 6 a, Examples of lasing spectra of the normal lung tissue (5 μm in thickness) stained with YOPRO (0.1 mM) under various pump energy densities. b, Examples of lasing spectra of the lung cancer tissue (5 μm in thickness) stained with YOPRO (0.1 mM) under various pump energy densities. All curves are vertically shifted for clarity. Cavity length = 15 μm. Excitation wavelength = 470 nm. The measured FSR in both a and b is approximately 6.8 nm. The slight blueshift in a and b is the result of the photobleaching effect. c, Statistics of the cell lasing threshold for the 5 μm thick normal lung tissues from the same six patients used in Fig. 4. d, Statistics of the cell lasing threshold for the 5 μm thick lung cancer tissues from the same six patients used in Fig. 4. In particular, N1/T1, N2/T2, and N3/T3 were from match-paired patients whereas the rest were from different patients (non-matched patients). In c and d, each dot represents the lasing data from a single cell. Statistical box plots are also shown in the same figures.

range of 500–580 nm to provide optical feedback and high transmission around 470 nm for excitation. The *Q*-factor of the FP cavity was on the order of 10⁴ at a cavity length of 15 μm (in the absence of tissues).

The spacers were fabricated with negative photoresist SU8 on the surface of the top mirrors using standard soft lithography. The mirrors were first cleaned by solvent ultrasonication (sonicated in acetone, ethanol, and de-ionized water sequentially) and oxygen plasma treatment. Then, they were dried at 150 °C for 15 minutes right before a 15 μm thick SU8 2010 (MicroChem Corp., USA) layer was spin-coated on top. After soft-baking the SU8-coated mirrors for 1 minute at 65 °C and 4 minutes at 95 °C, a contact lithography tool Karl Suss MA 45S was used to UV expose the mirrors through a mask with a bar-like spacer design. The exposed mirrors were subsequently subjected to post-exposure baking at 65 °C for 1 minute and 95 °C for 5 minutes, followed by 4 minutes of development. After rinsing and drying, the SU8 spacer on top of the mirror could be clearly seen by the naked eye. The spacers were further hard baked at 150 °C for 10 minutes and treated with oxygen plasma to improve hydrophilicity.

Optical system setup

A typical confocal setup was used to excite the sample and collect emission light from the FP cavity (Fig. 1). In this work,

a pulsed optical parametric oscillator (OPO) laser (pulse width: 5 ns, repetition rate: 20 Hz) at 470 nm was used as the excitation source to excite the stained tissues with a laser beam size of 30 μm in diameter. The pump intensity was adjusted using a continuously variable neutral density filter, normally in the range of 10–300 μJ mm⁻². The emission light was collected through the same lens and sent to a spectrometer (Horiba iHR550, spectral resolution ~0.2 nm) for analysis.

All experiments were performed in compliance with the relevant laws and institutional guidelines. All the human tissues were obtained under IRB approved by the institutional committees and the informed consent forms were obtained.

3. Results

Fig. 1 illustrates the tissue laser platform, in which the FFPE tissue labeled with nucleic acid probes (such as YOPRO) is sandwiched inside an FP cavity formed by a bottom mirror and a removable top mirror. In particular, an SU8 spacer of 15 μm in height, slightly more than the tissue thicknesses used in this work, was microfabricated on the top mirror (Fig. S1†). Such a design ensures a fixed cavity length regardless of the tissue thickness. Consequently, consistent results can be obtained even when the top mirror is repetitively removed and placed back and when different tissue

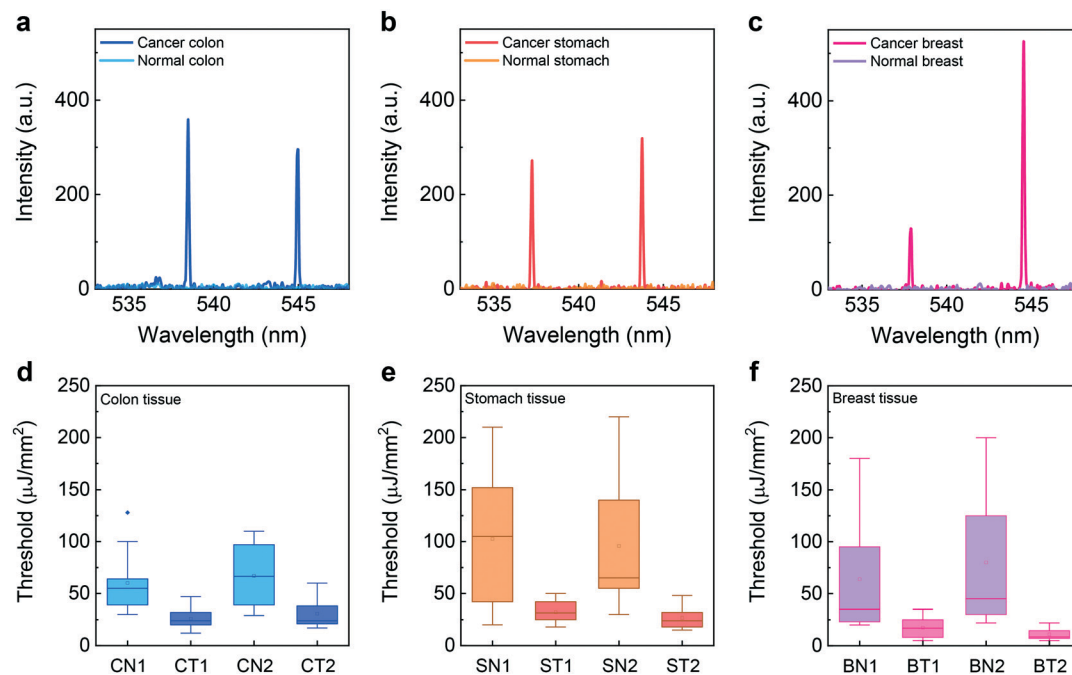


Fig. 7 a, Lasing spectra of cancer/normal colon cancer tissues measured under a pump energy density of $30 \mu\text{J mm}^{-2}$. b, Lasing spectra of cancer/normal stomach cancer tissues measured under a pump energy density of $30 \mu\text{J mm}^{-2}$. c, Lasing spectra of cancer/normal ductal breast cancer tissues measured under a pump energy density of $30 \mu\text{J mm}^{-2}$. Tissue thickness = $5 \mu\text{m}$. Cavity length = $15 \mu\text{m}$. d-f, Statistics of normal and tumor cell lasing thresholds from (d) colon ($N = 46$ cells), (e) stomach ($N = 42$ cells), and (f) breast tissues ($N = 52$ cells). For each type of tissue, two matched-paired patients' specimens were tested, labeled CN1 and CN2 (normal colon); SN1 and SN2 (normal stomach); BN1 and BN2 (normal breast) and CT1 and CT2 (colon tumor); ST1 and ST2 (stomach tumor); BT1 and BT2 (breast tumor). For each patient, a minimum of 10 cells were randomly selected and measured. Statistical box plots are also shown in d-f. The representative lasing threshold curves of the cancer tissues are given in Fig. S7.† The corresponding ROC curves are given in Fig. S8.†

thicknesses are used in the measurement. Furthermore, due to the gap between the tissue and the top mirror, the damage to the tissue and the top mirror is minimized. Details of the mirror fabrication and characterization can be found in the Experimental section and Fig. S1.† During the experiment, either tissue or the excitation laser is scanned to form laser emission-based images. In addition, since the top mirror is removable, the regular bright-field images and fluorescence images can be acquired and overlap with the laser emission images.²⁸

As an example given in the lower inset of Fig. 1, cancer cell nuclei present several highly concentrated nucleic acid sites (heterochromatins) that may provide a higher gain for lasing emission. Our earlier findings using cryogenic tissues showed that the cancer tissues (cells) have much lower lasing thresholds than the normal tissues (cells), which results from chromatin condensation and the increased levels of nucleic acid activities in malignant cell nuclei. This unique lasing characteristic allows us to distinguish cancer tissues from normal ones with high sensitivity and specificity (AUC = 99.8%).²⁰ Switching from cryogenic tissues to FFPE tissues causes two immediate consequences. First, the high scattering and opacity of FFPE tissues may preclude lasing at reasonable excitation. Second, chromatin or nucleic acids may degrade over time after being processed by the FFPE method. Therefore, the lasing threshold difference between the cancer and normal tissues may not be significant for observation. To

our relief, sharp lasing peaks were able to be achieved by using FFPE tissues stained with YOPRO. As a control experiment, we also tested the lasing possibility of pure YOPRO in Fig. S2.† No laser emission could be generated from YOPRO without binding to nucleic acids in the tissue. In contrast, the lasing spectra of $10 \mu\text{m}$ thick normal and cancer FFPE tissues stained with YOPRO under various pump energy densities are provided in Fig. 2a and b, respectively (exemplary H&E images are given in Fig. 2c). The spectrally integrated laser emission *versus* pump energy density for the cancer and normal tissues is presented in Fig. 2d, from which the lasing threshold is derived to be approximately $30 \mu\text{J mm}^{-2}$ and $72 \mu\text{J mm}^{-2}$, respectively. The significant difference in the lasing threshold can thus allow differentiation between the cancer and normal tissues/cells. For example, in Fig. 2e a sharp lasing peak can be only obtained in cancer cells with a high signal-to-background ratio at a pump energy density of $70 \mu\text{J mm}^{-2}$, whereas no lasing is observed in the normal tissue under the same pump energy density due to lower nucleic acid concentrations (*i.e.*, less gain from YOPRO) in the cell nucleus. Fig. 2f further shows representative lasing emission images taken from the normal and cancer tissues when pumped at $70 \mu\text{J mm}^{-2}$. No lasing emission is seen from the normal tissues, whereas strong lasing emission with superior contrast against the surrounding background is observed from the cell nuclei in the cancer tissue. When the pump

energy density is increased to $100 \mu\text{J mm}^{-2}$, multiple lasing cells at different sites can all be seen for both normal and cancer tissues. More examples of lasing emission images are provided in Fig. 2g.

In order to demonstrate that the designed spacer provides a robust laser cavity to generate reproducible lasing results, the time series lasing spectra of cancer and normal lung FFPE tissues are shown in Fig. 3a and b, respectively. The lasing spectra were measured intermittently over a 5 minute period. At $\tau = 1$ s, the free spectral range (FSR) in the cancer and normal tissues was 6.8 nm and 6.9 nm, respectively, which agree well with the theoretical calculation using eqn (1) at their respective lasing peak wavelength of 542 nm and 545 nm:

$$\text{FSR} = \frac{\lambda^2}{2n_1t + 2n_2(d-t)} \quad (1)$$

where $n_1 = 1.44$ and $n_2 = 1.42$ are the FFPE tissue refractive index^{29,30} and the matching refractive index of the oil, respectively, t is the sectioned tissue thickness within the cavity, and $d = 15 \mu\text{m}$ is the spacer height (cavity length). Note that the closely matched refractive indices between the tissue and the oil ensure that virtually no change in the FSR occurs when tissues of different thicknesses are used. Also note that the use of refractive index matching immersion oil between the tissue and the cover slip is a routine in conventional microscopy measurement. At $\tau = 300$ s, the FSR remains 6.8 nm for the cancer tissues and the peak position of lasing emission is consistent with that at $\tau = 1$ s, suggesting that the cavity length can be maintained throughout the experiment. This is a significant improvement over the FP cavity used in our previous work, in which the top mirror was in contact with the tissue. In that scenario, the cavity length is determined by the tissue thickness that varies from one sample to another and may even change during the measurement on the same sample (due to water evaporation, ice thawing, *etc.*). Similarly, as shown in Fig. 3b, a consistent FSR (and hence the cavity length) was also obtained for the normal tissue, despite a small blue shift of 0.45 nm that was likely caused by photobleaching due to high excitation. Multiple tissue sections (2 sections for each tissue from each patient) of $10 \mu\text{m}$ in thickness sliced from both lung cancer and normal FFPE blocks were further tested. Although there may exist a small tissue thick variation for each tissue, the FSR remains remarkably stable. As will be shown later, different tissue thicknesses (such as $5 \mu\text{m}$) and types (such as colon, stomach, and breast tissues) were also tested and the FSR again remains 6.8 nm–6.9 nm (depending on the lasing wavelength), which attests to the robustness and repeatability of our system. Note that due to the natural variation in the cell size and cell/nucleus refractive index, which causes a small change in the optical path of the FP cavity, the lasing emission wavelength may vary slightly. For example, the lasing wavelength is 542.00 nm and 545.64 nm, respectively, for the

right-hand peak in Fig. 3a and b, which corresponds to less than 1% change in the cavity optical path.

Taking advantage of this system, we systemically investigated the lasing thresholds of 14 patients' lung biopsies in Fig. 4, all of which were stained with 0.1 mM YOPRO. First, in Fig. 4a and b we present the statistics of lasing thresholds based on 3 pairs of normal and cancer FFPE tissues from the same patients, respectively. At least 15 cells were randomly selected and measured within each normal/tumor tissue region for each patient. All cancer cells exhibit consistently a narrow lasing threshold range between $50 \mu\text{J mm}^{-2}$ to $80 \mu\text{J mm}^{-2}$. In contrast, the normal cells have a much wider threshold range, varying from $50 \mu\text{J mm}^{-2}$ to $250 \mu\text{J mm}^{-2}$. Next, we investigated the lasing thresholds of normal and cancer FFPE tissues from 10 different patients (4 normal and 6 cancer) in order to examine the sample-to-sample variations. In particular, two types of non-small cell lung cancers (adenocarcinoma and squamous cell carcinoma) with different extents of differentiation were investigated. Exemplary H&E images are given in Fig. S3.† Similar statistic results of lasing thresholds are observed in Fig. 4c and d, regardless of the cancer subtype and differentiation. In comparison with cryogenic frozen tissues, FFPE tissues tend to have higher lasing thresholds in both normal and cancer tissues ($25 \mu\text{J mm}^{-2}$ vs. $60 \mu\text{J mm}^{-2}$ on average for the cancer tissues and $60 \mu\text{J mm}^{-2}$ vs. $100 \mu\text{J mm}^{-2}$ on average for the normal tissues), which is due to the higher scattering loss of the FFPE tissues. Nevertheless, the FFPE tissues can still lase at a threshold far below the tissue damage level.

Based on the results in Fig. 4, the histogram of the lasing thresholds is plotted in Fig. 5a. Apparently, the lasing thresholds for most cancer cells are below $80 \mu\text{J mm}^{-2}$ whereas those for the majority of normal cells are above that. The lower lasing thresholds in cancer cells are attributable to the higher DNA concentration in cancer cells resulting from higher proliferation and chromatin condensation,³¹ as we discussed previously.²⁰ In order to find the optimal excitation for cancer cell screening, we plot the receiver operation characteristic (ROC) curve in Fig. 5b by varying the excitation as the cut-off criterion and generate a fitted area under the curve of 0.87. The optimal excitation to distinguish cancer cells from the normal cells is found to be $80 \mu\text{J mm}^{-2}$, which corresponds to a sensitivity of 85.0%.

Our next task is to verify whether our system is compatible with the current practice in pathology, in particular, whether our system can accommodate thinner tissues. In a pathological lab, a tissue thickness of $5 \mu\text{m}$ is preferable, which helps save precious tissue samples. Therefore, in our experiment we reduced the FFPE tissue thickness from $10 \mu\text{m}$ to $5 \mu\text{m}$ and sandwiched them in the same cavity (with a $15 \mu\text{m}$ spacer). Since the top mirror was removable and there was a gap between the top mirror and the tissue, replacing tissue samples, which were mounted on the bottom mirrors, was quite straightforward. Fig. 6a and b are the examples of the lasing spectra from the $5 \mu\text{m}$ thick normal and cancer tissues labeled with YOPRO under various pump energy densities.

The FSR is measured to be approximately 6.8 nm for both tissues (considering the lasing peak wavelengths of 541 and 538 nm), which is consistent with the results obtained for the 10 μm thick tissues. In Fig. 6c and d, we selected 6 normal and 6 cancer lung tissues used in Fig. 4 and investigated their respective lasing thresholds. Overall, there is no statistical difference between the 5 μm and 10 μm samples. The corresponding ROC curve is plotted in Fig. S4,† showing the area under the curve of 0.9 and a sensitivity of 97.7% with an excitation cut-off criterion of 80 $\mu\text{J mm}^{-2}$. The above results suggest that our system is highly robust and is able to differentiate cancer and normal tissues/cells regardless of the tissue thickness.

Finally, we demonstrated that our platform and the findings are generally applicable to other types of tissues. This time, all the samples (5 μm in thickness) were prepared independently by technicians in Xi'an No. 3 Hospital in China using the bottom mirrors and the protocols provided by the University of Michigan team. The samples were shipped internationally and examined using the experimental setup described previously. First, we used the lung cancer tissues. Fig. S5† (tissue T10) shows the plot of the corresponding lasing threshold statistics, showing that it is very similar to the lasing threshold statistics obtained from the lung cancer tissue samples prepared by the University of Michigan team. Therefore, the identical experimental conditions (such as laser excitation spot size, repetition rate, laser scanning speed, spectrometer settings, *etc.*) used in Fig. 1–6 can be employed to test the samples from China. Fig. 7a–c show the exemplary lasing spectra measured from colon, stomach, and breast cancer/normal FFPE tissues (5 μm in thickness) labeled with YOPRO, respectively. Both the cancer and normal tissues were pumped under the same pump energy density of 30 $\mu\text{J mm}^{-2}$. Only lasing emission from cancer cells/tissue is observed since the pump energy density is below the lasing threshold for normal cells. Additionally, the measured FSR for each tissue is approximately 6.8 nm which matches well with the previous results, implying the reproducibility of such a lasing cavity. The exemplary H&E microscopy images as well as spectrally integrated laser emission *versus* pump energy density for respective tissues are presented in Fig. S6 and S7.† Based on the same procedures as before, we investigated the lasing thresholds for each type of tissue (normal and cancer), with 2 matched-pair patients for each in Fig. 7d–f. We observed that the lasing thresholds for the cancer tissue are relatively lower than the normal tissue among all three tissue types (mean thresholds for normal colon = 60 $\mu\text{J mm}^{-2}$, colon cancer = 25 $\mu\text{J mm}^{-2}$; normal stomach = 102 $\mu\text{J mm}^{-2}$, stomach cancer = 32 $\mu\text{J mm}^{-2}$; normal breast = 63 $\mu\text{J mm}^{-2}$; breast ductal cancer = 18 $\mu\text{J mm}^{-2}$). Interestingly, the normal colon tissue has a slightly lower lasing threshold compared to all, which could be explained by the high renewal rate of epithelial cells in colons.³² Yet, we are still able to distinguish between the colon cancer and normal tissues by their lasing thresholds. The ROC curves based on the data in Fig. 7d–f are plotted in Fig. S8,† which have an area under

the curve of 0.90, 0.88, and 0.95 for colon, stomach, and breast FFPE tissues, respectively. For all three types of tissues, a high sensitivity of 90.0% or above can be reached with the optimal excitation around 40–45 $\mu\text{J mm}^{-2}$.

4. Discussion and conclusion

In this work, we have addressed three possible roadblocks that may potentially impede the practical use of the laser emission-based detection/imaging technology: (1) compatibility with FFPE tissues; (2) robust system for reproducible results and protocol compatible with the practice in pathological labs, and (3) compatibility with a variety of tissue types. First, we have successfully achieved lasing in FFPE tissues and were able to differentiate cancer and normal tissues by their lasing thresholds. Second, we have developed a reliable system with a spacer microfabricated on the top mirror. As such, the cavity length is fixed, which allows generation of reproducible and stable results regardless of tissue thickness. The gap between the top mirror and the tissue makes it easy to exchange tissues without damaging them. Different tissue thicknesses were examined to demonstrate that our technology can be incorporated into the current practice in a pathological lab. Third, we showed that the lasing emission-based detection/imaging technology is applicable to other types of tissues. The results suggest that the platform and the related protocol are ready for tissue screening and cancer diagnosis studies on a larger scale.

In the near future, a few potential directions are worth pursuing. First, this platform can be broadly applied to fundamental biological research, especially for preclinical animal models, which require massive amounts of samples for data analysis. Besides cancer and normal tissues, it is also important to investigate the possibilities to differentiate benign and malicious tissues by using similar tools. Therefore a robust system with high reproducibility is necessary. Note that this platform is not limited to nucleic acid analysis. In fact, it can be extended to protein and peptide detection. Second, this system can be an ideal platform for tissue microarray analysis. Arrays of tissue biopsies containing tissue cores from different sources can be mounted on a single mirror to form a “tissue laser microarray”. This will allow high-throughput simultaneous lasing measurement and analysis of many tissue samples with minimal variations. Finally, a high-speed motor stage, a high repetition-rate pump laser, and a high-speed imager will be integrated to construct a wide-field automated laser-imaging system for rapid tissue analysis.

Author contributions

Y. C., Q. C., and X. F. conceived this research and designed the experiments; Y. C. performed the experiments; Q. C. fabricated the spacer; Y. C. and J. W. prepared the samples; X. W. and Y. C. drew the figures; Y. C., Q. C., J. W., X. T., and X. F. analyzed the data; Y. C. and X. F. wrote the paper.

Conflicts of interest

The authors declare no competing financial interests.

Acknowledgements

We acknowledge support from the National Science Foundation (ECCS-1607250).

References

- 1 X. Fan and S.-H. Yun, The potential of optofluidic biolasers, *Nat. Methods*, 2014, **11**, 141–147.
- 2 E. Ignesti, *et al.*, A new class of optical sensors: a random laser based device, *Sci. Rep.*, 2016, **6**, 35225.
- 3 M. Humar and S. H. Yun, Intracellular microlasers, *Nat. Photonics*, 2015, **9**, 572–576.
- 4 M. Schubert, *et al.*, Lasing within live cells containing intracellular optical micro-resonators for barcode-type cell tagging and tracking, *Nano Lett.*, 2015, **15**, 5647–5652.
- 5 M. C. Gather and S. H. Yun, Single-cell biological lasers, *Nat. Photonics*, 2011, **5**, 406–410.
- 6 Y. Wei, *et al.*, Starch-Based Biological Microlasers, *ACS Nano*, 2016, **11**(1), 597–602.
- 7 Y.-C. Chen, Q. Chen and X. Fan, Lasing in blood, *Optica*, 2016, **3**, 809–815.
- 8 X. Wu, *et al.*, Optofluidic laser for dual-mode sensitive biomolecular detection with a large dynamic range, *Nat. Commun.*, 2014, **5**, 3779.
- 9 P. L. Gourley, Biocavity laser for high-speed cell and tumour biology, *J. Phys. D: Appl. Phys.*, 2003, **36**, R228.
- 10 Y.-C. Chen, Q. Chen and X. Fan, Optofluidic chlorophyll lasers, *Lab Chip*, 2016, **16**, 2228–2235.
- 11 Q. Song, *et al.*, Random lasing in bone tissue, *Opt. Lett.*, 2010, **35**, 1425–1427.
- 12 C. P. Dietrich, *et al.*, An exciton-polariton laser based on biologically produced fluorescent protein, *Sci. Adv.*, 2016, **2**, e1600666.
- 13 M. Humar, A. Dobravec, X. Zhao and S. H. Yun, Biomaterial microlasers implantable in the cornea, skin, and blood, *Optica*, 2017, **4**, 1080–1085.
- 14 C. Vannahme, F. Maier-Flaig, U. Lemmer and A. Kristensen, Single-mode biological distributed feedback laser, *Lab Chip*, 2013, **13**, 2675–2678.
- 15 Q. Chen, A. Kiraz and X. Fan, Optofluidic FRET lasers using aqueous quantum dots as donors, *Lab Chip*, 2016, **16**, 353–359.
- 16 Q. Chen, *et al.*, Highly sensitive fluorescent protein FRET detection using optofluidic lasers, *Lab Chip*, 2013, **13**, 2679–2681.
- 17 Y. Sun and X. Fan, Distinguishing DNA by Analog-to-Digital-like Conversion by Using Optofluidic Lasers, *Angew. Chem., Int. Ed.*, 2012, **51**, 1236–1239.
- 18 S. Cho, M. Humar, N. Martino and S. H. Yun, Laser Particle Stimulated Emission Microscopy, *Phys. Rev. Lett.*, 2016, **117**, 193902.
- 19 Y.-C. Chen, Q. Chen, T. Zhang, W. Wang and X. Fan, Versatile tissue lasers based on high-Q Fabry-Pérot microcavities, *Lab Chip*, 2017, **17**, 538–548.
- 20 Y.-C. Chen, *et al.*, Laser-emission imaging of nuclear biomarkers for high-contrast cancer screening and immunodiagnosis, *Nat. Biomed. Eng.*, 2017, **1**, 724–735.
- 21 Y. Wang, *et al.*, Random lasing in human tissues embedded with organic dyes for cancer diagnosis, *Sci. Rep.*, 2017, **7**, 8385.
- 22 R. Polson and Z. V. Vardeny, Cancerous tissue mapping from random lasing emission spectra, *J. Opt.*, 2010, **12**, 024010.
- 23 M. K. Creech, J. Wang, X. Nan and S. L. Gibbs, Superresolution Imaging of Clinical Formalin Fixed Paraffin Embedded Breast Cancer with Single Molecule Localization Microscopy, *Sci. Rep.*, 2017, **7**, 40766.
- 24 J. Weißer, *et al.*, Quantitative proteomic analysis of formalin-fixed, paraffin-embedded clear cell renal cell carcinoma tissue using stable isotopic dimethylation of primary amines, *BMC Genomics*, 2015, **16**, 559.
- 25 N. Tanaka, *et al.*, Whole-tissue biopsy phenotyping of three-dimensional tumours reveals patterns of cancer heterogeneity, *Nat. Biomed. Eng.*, 2017, **1**, 796.
- 26 Y. Guo, *et al.*, RNA sequencing of formalin-fixed, paraffin-embedded specimens for gene expression quantification and data mining, *Intl. J. Genomics*, 2016, **2016**, 9837310.
- 27 A. Ly, *et al.*, High-mass-resolution MALDI mass spectrometry imaging of metabolites from formalin-fixed paraffin-embedded tissue, *Nat. Protoc.*, 2016, **11**, 1428–1443.
- 28 Q. Chen, *et al.*, An integrated microwell array platform for cell lasing analysis, *Lab Chip*, 2017, **17**, 2814–2820.
- 29 M. Xu, Plum pudding random medium model of biological tissue toward remote microscopy from spectroscopic light scattering, *Biomed. Opt. Express*, 2017, **8**, 2879–2895.
- 30 V. V. Tuchin, Optical clearing of tissues and blood using the immersion method, *J. Phys. D: Appl. Phys.*, 2005, **38**, 2497.
- 31 N. D. Magee, *et al.*, Raman microscopy in the diagnosis and prognosis of surgically resected nonsmall cell lung cancer, *J. Biomed. Opt.*, 2010, **15**, 026015.
- 32 E. E. Deschner, Cell turnover and colon tumor development, *Prev. Med.*, 1987, **16**, 580–585.